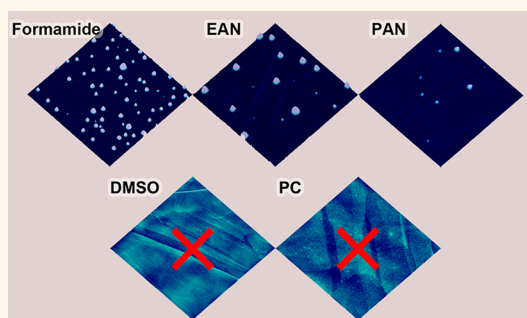


Surface Nanobubbles in Nonaqueous Media: Looking for Nanobubbles in DMSO, Formamide, Propylene Carbonate, Ethylammonium Nitrate, and Propylammonium Nitrate

Hongjie An,[†] Guangming Liu,[‡] Rob Atkin,[§] and Vincent S. J. Craig^{*,†}

[†]Department of Applied Mathematics, Research School of Physical Sciences and Engineering, Australian National University, Canberra, Australian Capital Territory 2601, Australia, [‡]Department of Chemical Physics, Hefei National Laboratory for Physical Sciences at the Microscale, University of Science and Technology of China, Hefei, P.R. China 230026, and [§]Discipline of Chemistry, University of Newcastle, Callaghan, New South Wales 2308, Australia

ABSTRACT Surface nanobubbles produced by supersaturation during the exchange of ethanol for water are routinely observed on hydrophobic surfaces, are stable for days, and have contact angles that are very much greater than observed macroscopically. Here, we test the hypothesis that nanobubbles can also be observed in nonaqueous solvents in order to ascertain if their anomalous lifetimes and contact angles are related to properties of the solvent. Nanobubbles were seen in the protic solvents formamide, ethylammonium nitrate, and propylammonium nitrate, but not in propylene carbonate or dimethyl sulfoxide. Solvents in which nanobubbles were observed exhibit a three-dimensional hydrogen-bonding network. Like in aqueous systems, the nanobubbles were stable for days and exhibited high contact angles ($\sim 165^\circ$).



KEYWORDS: nanobubbles · nonaqueous · ionic liquid · formamide · EAN · PAN · DMSO

Surface nanobubbles are gaseous entities trapped on immersed surfaces tens of nanometres in height. They were proposed to explain anomalously large attractive forces between hydrophobic surfaces immersed in aqueous solutions¹ and were first directly imaged by Atomic Force Microscopy (AFM) in 2000.^{2,3} Despite numerous investigations, two properties of surface nanobubbles are not adequately explained.^{4,5} The first is their stability. The curvature of the nanobubble interface leads to a high internal Laplace pressure that increases the solubility of the gas in the surrounding solution and the bubble shrinks by diffusion of gas into solution. Calculations show that the lifetime of nanobubbles should be much less than a second,^{6,7} which is 3–5 orders of magnitude shorter than the observed lifetimes.^{8–10} Supplementary theories have been proposed for the stability of nanobubbles such as the presence of a contaminant layer that either inhibits gas

transport or results in a surface pressure that counteracts the surface tension.^{9,11} While both effects are possible, it has been demonstrated that in the majority of studies such contaminants are not present; bubble stability is retained even when surfactant is added to remove any contaminants.^{10,12} Recently, several researchers have invoked contact line pinning as a stabilizing mechanism^{8,13–15} whereby a shrinking nanobubble that remains pinned will exhibit a progressively higher contact angle (measured through the more dense phase) and consequently a reduced radius of curvature and lower Laplace pressure. However, not all long-lived nanobubbles exhibit strong contact line pinning,¹⁶ nanobubble growth and shrink rates are similar, and there are reports that bulk nanobubbles are stable for days.^{5,17–23} Explanations that rely on the properties of a solid surface cannot explain these reports.

The second property that requires explanation is that surface nanobubbles have

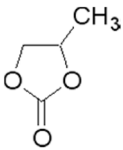
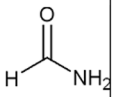
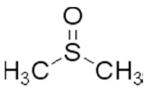
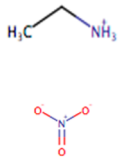
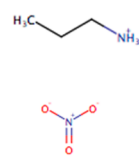
* Address correspondence to vince.craig@anu.edu.au.

Received for review May 13, 2015 and accepted July 8, 2015.

Published online July 08, 2015 10.1021/acsnano.5b02915

© 2015 American Chemical Society

TABLE 1. Physical Properties of Selected Nonaqueous Solvents^a

Solvent	Water	Propylene carbonate	Formamide	Dimethylsulfoxide (DMSO)	Ethylammonium Nitrate	Propylammonium Nitrate
Abbreviation		PC		DMSO	EAN	PAN
Formula	H ₂ O	C ₄ H ₆ O ₃ 	HCONH ₂ 	(CH ₃) ₂ SO 	(C ₂ H ₅)NH ₃ ⁺ .NO ₃ ⁻ 	(C ₃ H ₇)NH ₃ ⁺ .NO ₃ ⁻ 
Protic	Yes	No	Yes	No	Yes	Yes
Dielectric Constant (20°C)	80.20	66.14	110.0	47.24	26.2 ⁴⁶	
Viscosity (mPa s) (25°C)	0.890	2.5 ⁴⁷	3.30	1.987	35 ⁴⁸	105 ⁴⁸
Surface tension (mN m ⁻¹) (25°C)	71.99	41.9 (20°C) ⁴⁹	57.03	42.92	49.5 ⁴⁸	40.0 ⁴⁸

^a All data taken from Handbook of Chemistry and Physics,⁵⁰ except where otherwise referenced.

anomalously high contact angles. Here, we adopt the established convention of describing the contact angle as the arc measured through the denser (in this case liquid) fluid phase. The nanobubble contact angle is typically 50–80° higher than that for macroscopic bubbles at the same solid–liquid interface.²⁴ These exceptional contact angles cannot be explained by line tension, imaging artifacts, contamination, contact angle hysteresis, or out of equilibrium effects.²⁵ The presence of a gaseous surface layer has also been proposed as a reason for the exceptionally high nanobubble contact angles. However, it is unclear how the presence of a gas film leads to an elevated contact angle or why the effect is not observed for macroscopic bubbles²⁶ as short-range (<10 nm) interactions determine the contact angle.

Interest in nanobubble research stems from the challenge of understanding their origin and properties, their possible use in applications such as cleaning,^{27–30} environmental remediation,³¹ water treatment,³² plant growth,²⁰ and medicine,^{33–36} and because their presence may interfere with surface science investigations and be problematic in industrial applications. For example, nanobubbles on surfaces will cause defects in electroplated surfaces and alter the slip properties of surfaces.^{37,38}

Surface nanobubbles are typically produced on hydrophobic surfaces by a process that results in supersaturation of the solvent such as electrolysis, turbulent mixing, or solvent exchange. During solvent exchange, the surface is initially immersed in a water miscible solvent that has a high level of dissolved gas

such as ethanol. At this stage, no nanobubbles are observed. The solvent is then displaced with water. During displacement of ethanol with water, mixing occurs, resulting in gas supersaturation and nucleation of nanobubbles. To date, nanobubbles have only been reported in solutions which are aqueous or aqueous mixtures,³⁹ with the exception of the work done with alcohols by Simonsen and co-workers which is usually discounted because other groups have been unable to repeat these results.⁴⁰ Here, we test the hypothesis that nanobubbles can be produced in nonaqueous solutions to ascertain whether water plays a significant role in nanobubble stability and if the exceptional contact angles obtained in water are reproduced in nonaqueous solvents. We have chosen the solvents dimethyl sulfoxide (DMSO), propylene carbonate (PC), formamide, ethylammonium nitrate (EAN), and propylammonium nitrate (PAN) as they exhibit moderate to high contact angles on hydrophobic substrates, are miscible with ethanol, and because they represent a wide range of solution properties. EAN and PAN are nanostructured^{41,42} protic ionic liquids (ILs) that have extensive hydrogen bond networks.⁴³ The transfer of rare gases and hydrocarbons from cyclohexane to EAN is accompanied by negative enthalpy and entropy values similar to water.⁴⁴ Formamide has a 3-dimensional hydrogen bonding network similar to water,⁴⁵ whereas neat PC and DMSO do not have a hydrogen bonding network, nor does ethanol, the solvent exchange fluid of choice. Selected solvent physical properties are summarized in Table 1.

TABLE 2. Contact Angles of Selected Nonaqueous Solvents on Highly Ordered Pyrolytic Graphite

solvent	water	propylene carbonate	formamide	dimethyl sulfoxide (DMSO)	ethylammonium nitrate	propylammonium nitrate
Contact Angle on HOPG	$72 \pm 11^\circ$	$31 \pm 4^\circ$	$68 \pm 5^\circ$	$45 \pm 3^\circ$	$65 \pm 6^\circ$	$62 \pm 5^\circ$

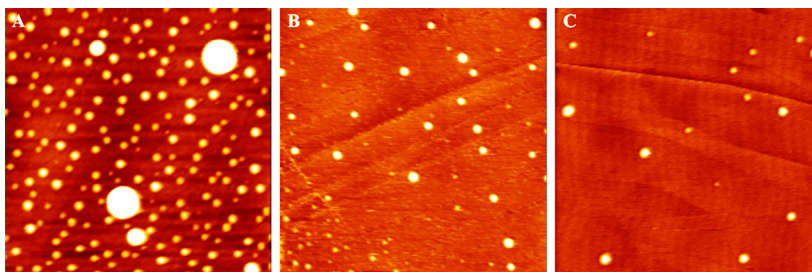


Figure 1. Tapping mode AFM height images of nanobubbles formed by solvent exchange on HOPG in formamide (A), EAN (B), and PAN (C). Image size, $5 \mu\text{m} \times 5 \mu\text{m}$; height scale, 20 nm.

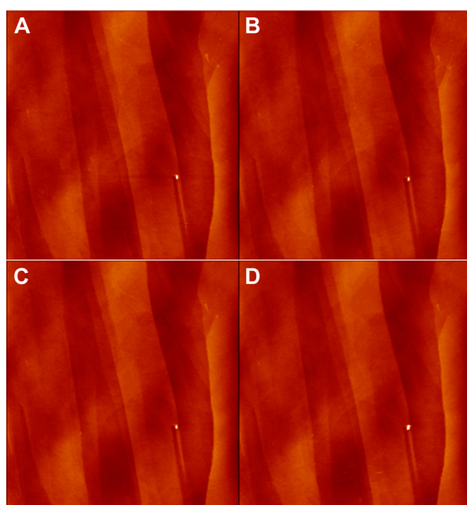


Figure 2. Tapping mode AFM height images of HOPG in ethanol before solvent exchange (A), in DMSO, after ethanol was displaced by DMSO (B), in DMSO after a second displacement of ethanol by DMSO (C), and in DMSO after a third displacement of ethanol by DMSO (D). No evidence of nanobubbles was observed. Image size, $10 \mu\text{m} \times 10 \mu\text{m}$; height scale, 20 nm.

RESULTS

Nanobubbles on HOPG in Nonaqueous Solvents. HOPG is a commonly used substrate for nanobubble imaging. We chose HOPG as a substrate in this study as it is a low energy surface that gives rise to moderately high contact angles for the chosen solvents. It is also very smooth, consisting of atomically flat terraces. The measured macroscopic contact angles on HOPG are summarized in Table 2.

Nanobubbles were observed in formamide, EAN, and PAN. Typical tapping mode height images obtained in these solvents are shown in Figure 1. The nanobubbles in formamide are similar in size to those seen in aqueous solutions. In comparison, the nanobubbles observed in EAN and PAN are considerably smaller. We note that nanobubbles in EAN and PAN

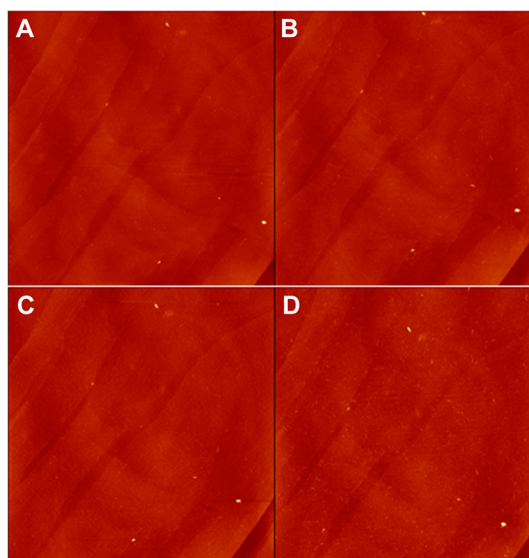


Figure 3. Tapping mode AFM height images of HOPG in ethanol before solvent exchange (A), in propylene carbonate after ethanol was displaced by propylene carbonate (B), in propylene carbonate after a second displacement of ethanol by propylene carbonate (C), and in propylene carbonate after a third displacement of ethanol by propylene carbonate (D). No evidence of nanobubbles was observed. Image size, $5 \mu\text{m} \times 5 \mu\text{m}$; height scale, 20 nm.

may not always be seen on HOPG, because of the difficulty in obtaining images in high viscosity media. The results were repeatable, provided the solvent exchange process was conducted very slowly (1 mL/min). In contrast, nanobubbles were not observed in DMSO and PC, as demonstrated in Figures 2 and 3. Note that we have previously observed nanobubbles in DMSO, but this was only when PDMS was added to explore the role of this contaminant.²⁵ It is currently unclear what role PDMS might play in the formation and stability of nanobubbles. When degassed ethanol or degassed formamide was used during solvent exchange, no nanobubbles were formed.

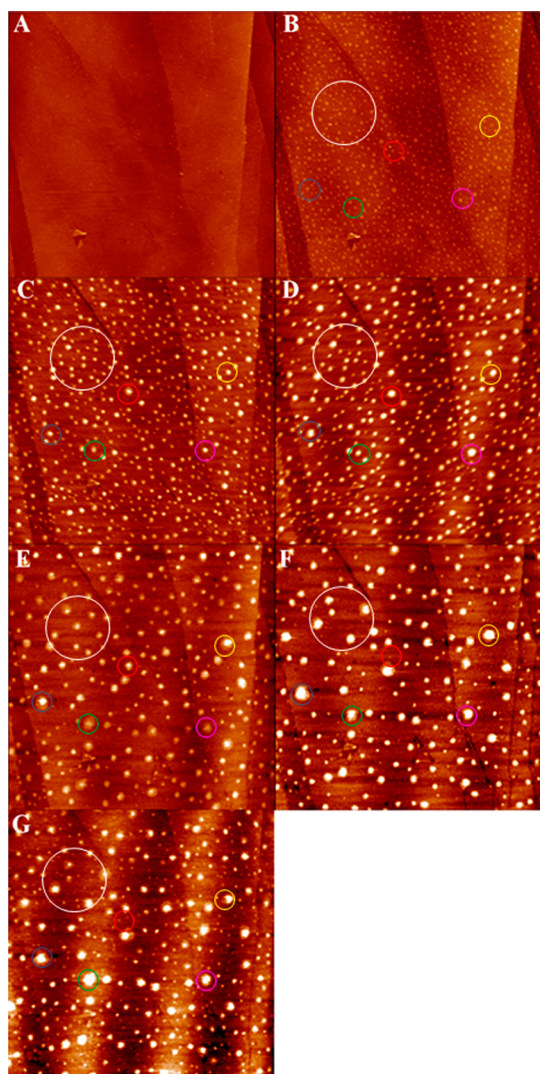


Figure 4. Nanobubbles in formamide on HOPG imaged at successive times. (A–D) On day 1 at 5 min, 30 min, 2 h, and 6 h, respectively; (E) 24 h, (F) 72 h, and (G) 120 h. Image size, $5\ \mu\text{m} \times 5\ \mu\text{m}$; height scale, 5 nm.

Stability of Surface Bubbles in Formamide. Having observed nanobubbles in formamide, their stability was investigated. After the formation of bubbles, the AFM system was left undisturbed for several hours and the surface was imaged periodically, see Figure 4. A closed fluid cell was used, so losses due to evaporation were minimal. Nanobubble sizes were observed to fluctuate over time and nanobubbles were still present on the surface after 5 days. Interestingly, no bubbles were observed 5 min after solvent exchange (Figure 4A). After this period, complete images could not be obtained for a period, due to poor imaging conditions associated with reduction in the oscillation amplitude of the cantilever. High quality images were not obtained until 30 min after solvent exchange (Figure 4B). This image revealed surface nanobubbles that grew with time.

The surface density of nanobubbles significantly decreased with time. In the area indicated by the white

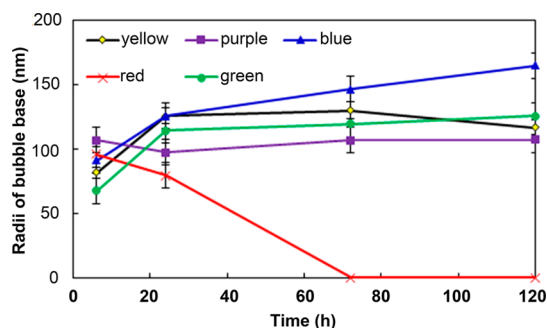


Figure 5. Evolution of the radius of selected bubble bases over time. Five bubbles were randomly selected. These are circled with different colors in Figure 4D–G.

circle in Figure 4, the bubble count was 46 at 5 min, 31 at 2 h, 20 at 6 h, 10 at 24 h, and only 5 at 72 h. Five bubbles were randomly chosen as indicated by the colored circles. Over time some bubbles shrank, while others grew. The bubble in the red circle grew from hour 2 to hour 6 and then shrank between hour 6 and hour 24, and disappeared by hour 72 (Figure 4C–F). The radius of the bubble base *versus* time is presented in Figure 5. Bubbles in the blue and green circles grew throughout the observation period, while the bubble in the yellow circle first grew and then shrank. The bubble in the purple circle first shrank and then grew and then became stable. The apparent size of soft objects can be influenced by changes in the imaging conditions. However, this can be discounted as the origin of the observed trends of bubble sizes in the images because the imaging conditions are constant within each image and the changes in bubble size observed are different for different nanobubbles. After 72 h, numerous smaller nanobubbles appeared (Figure 4G).

Morphology of Nanobubbles. Statistical analysis of the nanobubble morphology in formamide is shown in Figure 6. The height of nanobubbles in formamide ranged from several nanometers to 70 nm (mean = 15 nm, Gaussian width = 8.5 nm). The height of nanobubbles in the ILs were fit with a Gaussian distribution and were found to be very similar (EAN: mean = 15 nm, Gaussian width = 3 nm. PAN: mean = 15 nm, Gaussian width = 4 nm). The radius of the bubble base was found to be <250 nm in formamide, EAN, and PAN, which is less than usually observed in aqueous systems. A Gaussian distribution was fit to the bubble base radius in formamide (mean = 64 nm, Gaussian width = 29 nm).

Nanoscope contact angles of nanobubbles on HOPG in formamide were deduced from TM-AFM height images as described by Zhang.¹⁰ Figure 7 shows the nanoscopic contact angles calculated from the topography of 100 nanobubbles yielding $168 \pm 6^\circ$ for formamide, $156 \pm 5^\circ$ for EAN, and $165 \pm 4^\circ$ for PAN. All the measured nanoscopic contact angles are much higher than the macroscopic contact angles measured using a contact angle goniometer on HOPG: $68 \pm 5^\circ$ for

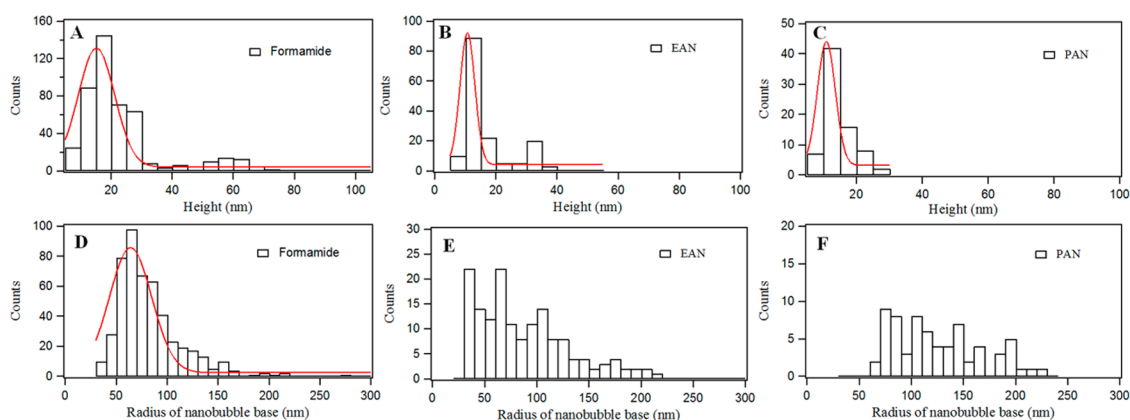


Figure 6. Distribution of height (A–C) and radius of bubble base (D–F) in formamide (A and D, $n = 499$), EAN (B and E, $n = 154$), and PAN (C and F, $n = 69$).

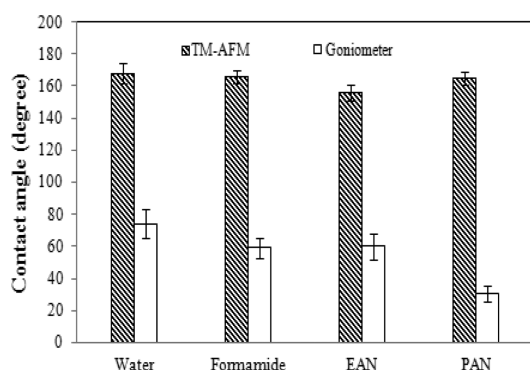


Figure 7. Measured nanoscopic and macroscopic contact angles of nanobubbles in formamide, EAN, and PAN on HOPG. Contact angles of water on HOPG are included here for comparison (data from Zhang¹⁰).

formamide, $65 \pm 6^\circ$ for EAN, $62 \pm 5^\circ$ for PAN. The nanoscopic contact angle results are very similar to those previously measured for nanobubbles in water ($168 \pm 9^\circ$).¹⁰

Nanomechanical Properties of Surface Bubbles in Formamide. To provide spatially resolved measurements of mechanical properties, Force–Volume (FV) imaging was employed to map the stiffness and adhesion of the HOPG surface and the nanobubbles. In this study, nanobubbles in formamide were visualized by TM-AFM, and the imaging mode was then changed to FV mode. The data is presented in Figure 8. A TM-AFM image of the region of interest is shown in Figure 8A. The image shown was captured after FV mapping had been performed in order to confirm that FV imaging did not alter the nanobubbles being imaged. FV imaging allows images to be produced from different slices of the deflection data. FV images are shown in Figure 8B,C using data obtained on approach and retraction (respectively) constructed from data at the force indicated by the arrows in Figure 8D and Figure 8E. At these locations on the deflection–displacement curves, the displacement is considerably different when a nanobubble is present compared to

the bare HOPG surface. This is what gives rise to the contrast between nanobubble-populated regions and the substrate in the FV images and also explains why the contrast is reversed between approach and separation.

Force *versus* distance data obtained for three different bubbles in formamide on approach are shown in Figure 8F and upon separation in Figure 8G. The nature of the raw data strongly indicates that at high force the tip of the cantilever pushes through the nanobubble and makes contact with the HOPG substrate. This allows contact between the HOPG surface and the cantilever to be defined and the separation measured relative to this value. The smaller nanobubbles show a linearly increasing repulsion on approach until close to contact. As there is no significant jump to contact, this is attributed to deformation of the nanobubble interface. The larger nanobubble (#1) exhibits the same initial linear repulsion before presenting a more complex force–separation. This more complex region indicates that the AFM tip is penetrating the bubble surface. The interfacial tension of the nanobubble surface in formamide can be calculated from the linear region when the force is measured in the center of the bubble.¹⁰ The interfacial tension was determined in this manner to be ~ 55 mN/m for the first regime of bubble #1; this is comparable with the literature value of 58 mN/m⁵¹ and indicates that the formamide–nanobubble interface is clean. Note this is evidence that the objects are indeed nanobubbles as an oil phase would give a much lower surface tension. Further evidence that nanobubbles are gaseous using fluorescence quenching has recently been reported.⁵²

In addition to HOPG, a fluorinated silicon wafer (PFOTS) was used as a substrate. A fluorinated surface was chosen for solvophobicity, which should enhance the propensity for nanobubble formation. Nanobubbles on the PFOTS surface were produced in formamide using the solvent exchange technique. However, it proved impossible to obtain clear images of these nanobubbles as they were mobilized by interaction

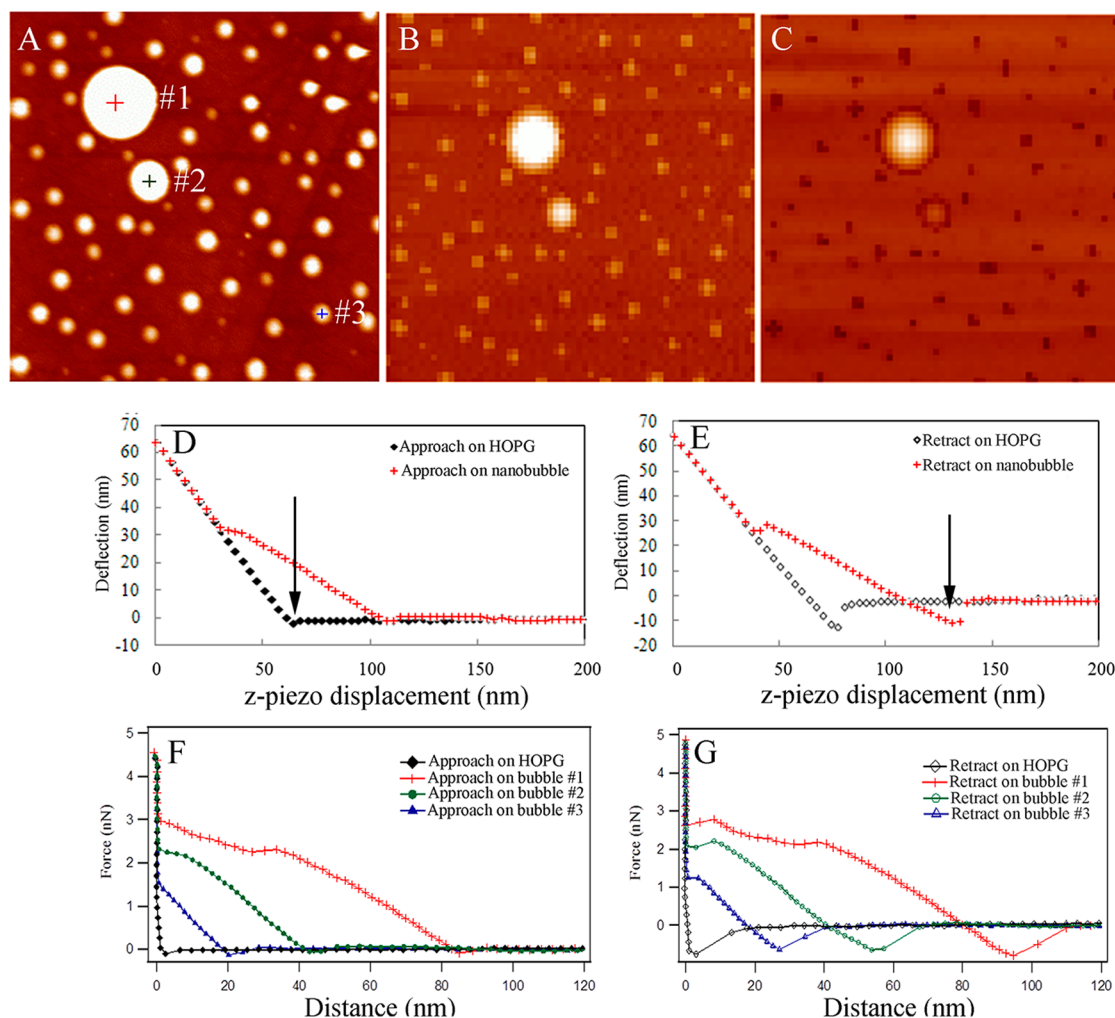


Figure 8. Nanomechanical properties of nanobubbles. **A** tapping mode image of the region of interest is shown in panel **A**. Force volume images of the same region are shown in panels **B** and **C**. The force volume data was obtained from complete force curve cycles mapped across the scan area. Images produced from approach and separation are mapped in panels **B** and **C**, respectively, over an area of $3\ \mu\text{m} \times 3\ \mu\text{m}$ with a z -scale of 50 nm. Examples of the piezo displacement–deflection data used to produce these images are shown in panels **D** and **E**, respectively. These panels compare the deflection vs z -piezo displacement measured on HOPG and nanobubbles. Panels **F** and **G** are force–separation curves on three nanobubbles (labeled #1, #2, and #3 in panel **A**) compared to the bare HOPG surface. The cantilever spring constant was 0.08 N/m.

with the AFM tip. This can be seen in Figure 9. Here, the slow scan direction is from top to bottom. Initially, two nanobubbles are imaged at the top; however, the rest of the image exhibits streaks, which are due to the movement of nanobubbles across the surface.

DISCUSSION

Our measurements reveal surface nanobubbles in formamide, EAN, and PAN like those found in aqueous solutions. Nanobubbles were not observed in propylene carbonate or DMSO. Furthermore, the nanobubbles in formamide were observed for 120 h, indicating that the extended stability of nanobubbles observed in aqueous solutions is also observed in formamide. We can conclude that the stability of surface nanobubbles is not unique to water and is therefore not due to a unique property of water.

As nanobubbles were not observed in all solvents in this study, it is valuable to consider what property of the solvent is important for the observation of surface nanobubbles. Inspection of Table 1 reveals that the solvents in which nanobubbles were observed, formamide, EAN, and PAN, are all protic solvents (as is water), whereas the other solvents are not. This suggests that a hydrogen-bonding network may be significant in stabilizing surface nanobubbles. We also note that it is generally accepted that nanobubbles are not seen in neat ethanol, which is also a hydrogen bonding solvent but it forms linear hydrogen bonded networks as opposed to a three-dimensional hydrogen-bonding network.⁵³ This may be due to the fact that ethanol wets the substrate and that a solvent with a significantly higher degree of dissolved gas than ethanol has not been employed in the solvent exchange process

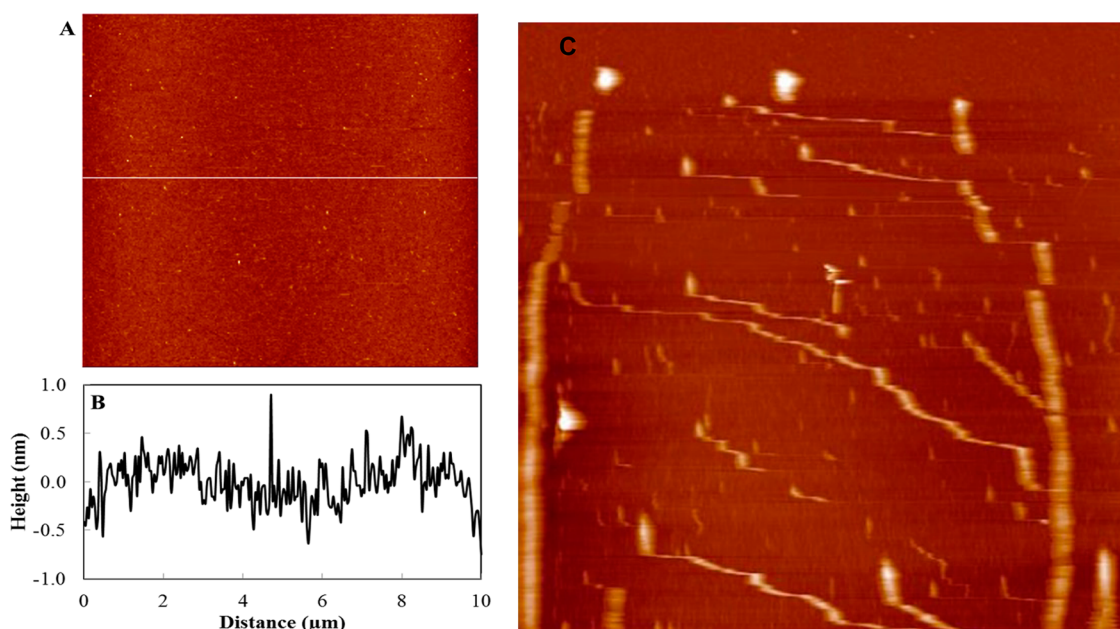


Figure 9. AFM images using a perfluorooctyltrichlorosilane treated silicon wafer (PFOTS). A tapping mode AFM image of the PFOTS surface is shown in panel A in air. Image size, $10\ \mu\text{m} \times 10\ \mu\text{m}$; height scale, 5 nm and a profile of the cross section at the position of the white line showed in panel A is shown in Panel B. The RMS roughness was measured at 0.23 nm, which is unchanged from the underlying silicon wafer. Tapping mode images of nanobubbles on a PFOTS surface immersed in formamide are shown in panel C. The features in the image are caused by nanobubbles; the lines are an artifact that arises from the mobility of the nanobubbles. The interaction with the AFM tip causes them to move during imaging making imaging extremely difficult. This was the best image obtained for this system. Image size, $10\ \mu\text{m} \times 10\ \mu\text{m}$; height scale, 50 nm.

with ethanol. With the exception of ethanol, the protic solvents studied have higher surface tensions than the aprotic solvents, and consequently, they have higher contact angles on HOPG. In aqueous systems, it is recognized that nanobubbles are formed easily on hydrophobic surfaces and with difficulty, or not at all, on hydrophilic surfaces. Therefore, it is possible that nanobubbles were not observed in DMSO and PC because the HOPG is not sufficiently solvophobic in these solvents.

Contact Angles of Surface Nanobubbles in Nonaqueous Solvents. The measured nanoscopic contact angles ($168 \pm 6^\circ$ for formamide, $156 \pm 5^\circ$ for EAN, and $165 \pm 4^\circ$ for PAN) are within error equivalent to the nanoscopic contact angles measured in water ($168 \pm 9^\circ$), but they are much higher than the macroscopic contact angles ($68 \pm 5^\circ$ for formamide, $65 \pm 6^\circ$ for EAN, $62 \pm 5^\circ$ for PAN, and $72 \pm 11^\circ$ for water) on HOPG. This indicates that the anomalous contact angles observed are not attributable to a unique property of water or a unique interaction between water and the HOPG surface. This infers that explanations that rely on the presence of a gaseous layer on the HOPG surface can only be correct if similar gaseous layers are also present in formamide, EAN, and PAN. We currently have no satisfactory explanation for the anomalously high contact angles observed for nanobubbles in these solvents or in water.²⁵

Temporal Stability of Surface Nanobubbles. The data presented in Figures 4 and 5, demonstrate that surface

nanobubbles in formamide survived for at least 120 h after production. This is comparable to the lifetimes of surface nanobubbles in water. This both confirms the earlier work and demonstrates that the stability of nanobubbles is not a unique property of nanobubbles in water. The time scale of stability is many orders of magnitude longer than the theoretically expected lifetime based on pressure induced solubility and diffusion.^{4,6,7} The changes that nanobubbles undergo over time are complex. Some bubbles grow, others shrink and the images suggest that some adjacent bubbles may even coalesce, but this process is not observed. This is consistent with previous observations of nanobubbles in water and evidence that the nanobubble interface is permeable.¹⁶ We attribute the different growth patterns of individual nanobubbles to differences in the local environment of each nanobubble. Nanobubbles with a permeable interface will influence the surrounding gas concentration and thereby will influence neighboring nanobubbles. At sufficient levels of supersaturation, nanobubbles become thermodynamically stable against shrinkage. We have calculated the radius of curvature of nanobubbles in formamide and found that most lie between 400 and 1000 nm. With a surface tension of $0.057\ \text{N m}^{-1}$, the level of saturation required to prevent dissolution is 2.15–3.80. Calculations below show that similar saturation levels may be produced during solvent exchange. However, supersaturation alone cannot explain the observed stability, because theory

predicts that any bubble that has a curvature not matched precisely to the saturation level should rapidly shrink or grow, suggesting that the kinetics of dissolution are much slower than expected based on diffusion alone.

Contact Line Pinning. Young's equation describes the equilibrium contact angle for a perfectly smooth and homogeneous surface. Real solid surfaces do not meet these criteria, and therefore, almost always exhibit contact angle hysteresis. The quasi-static advancing and receding contact angles differ because the three-phase line is said to be "pinned". Pinning arises because roughness and heterogeneity in the region of the three-phase line (TPL) can lead to energy barriers sufficient to prevent movement of the TPL. In the absence of contact angle hysteresis, a slowly shrinking nanobubble would maintain a constant contact angle. In contrast, a nanobubble that is strongly pinned, such that the TPL does not move at all, will exhibit an increasing contact angle (measured through the liquid phase) and an increasing radius of curvature during shrinking. The long lifetime of surface nanobubbles has been ascribed to pinning of contact lines,^{8,13–15} because a strongly pinned nanobubble will eventually achieve thermodynamic stability (with regard to solubility) with any solution that is slightly supersaturated. In the case of a shrinking nanobubble in solution, pinning will occur on sites that are least favorable for the solvent, whereas a growing nanobubble would be pinned on sites that are most favorable for the solvent. A further, and common, scenario is where the surface exhibits moderate pinning. In this case, the TPL will initially be pinned, but as the nanobubble continues to shrink, the TPL eventually becomes depinned and moves rapidly to a new position. During this rapid depinning, the area of the base of the nanobubble is reduced, but the volume is essentially constant. Consequently, depinning is *always* accompanied by a decrease in the radius of curvature of the nanobubble. Thus, any stability conferred by pinning is lost when depinning occurs and only resumes when the nanobubble becomes and continues to be pinned and further shrinkage results in an increase in the radius of curvature. The expectation from the increased Laplace pressure following depinning is that during this process the nanobubble should lose gas by diffusion in accord with Epstein–Plesset theory.⁶ Thus, a nanobubble can only be stabilized against dissolution for long periods by pinning if it remains strongly pinned at some stage. Moreover, all nanobubbles concurrently exhibiting long-term stability should have radii of curvature that are the same if the stability is ascribed to pinning.

In this study, nanobubbles on PFOTS surfaces were found to be very mobile (see Figure 9). This indicates that pinning was overcome by the mechanical disturbance of the cantilever. As described above, depinning removes any stabilization previously gained

through pinning. The disturbed nanobubbles did not shrink or grow rapidly, which indicates that pinning is not responsible for the stabilization of nanobubbles in formamide on PFOTS. Additionally, some nanobubbles were seen to grow, and in this case, pinning will decrease the radius of curvature of the nanobubble and increase the Laplace pressure. Therefore, for growing nanobubbles, pinning fails to provide a stabilization mechanism. Previous research showed that nanobubbles on micropatterns can be relocated by AFM tips in DMSO without any effect on their stability.²⁵ A fluid on a liquid surface cannot be pinned; therefore, this is another example of a nanobubble where pinning does not provide an explanation for the stability. This rules out pinning as a universal means by which surface nanobubbles are stabilized.

Solvent Exchange. As the surface nanobubbles in this study are produced by solvent exchange, it is instructive to evaluate this poorly understood process. It is generally accepted that the essential outcome of solvent exchange for the production of nanobubbles is mixing of pure saturated miscible solvents that results in a supersaturation of gas in the mixture. In the case of ethanol–water solvent exchange, the solubility of gas is much higher in ethanol than in water. As the data is available for the solubility of nitrogen in ethanol/water mixtures, it is possible to calculate the level of supersaturation that can be achieved by mixing the saturated solvents at different mole fractions; this is shown in Figure 10. What is apparent is that even though nitrogen gas is ~27 times more soluble in ethanol than water, the maximum nitrogen saturation level that can be achieved upon mixing is 285%. The maximum arises as at high water fraction, the amount of gas contributed from the ethanol phase is small, and at high ethanol fraction, nitrogen has a high solubility in the mixture. Calculations for nitrogen solubility in 2-propanol/water mixtures show similar behavior and approximately the same maximum in obtainable saturation.

This calculation ignores the temperature change due to the enthalpy of mixing. The largest temperature change on mixing for any mixture of ethanol and water at room temperature can be determined from the enthalpy of mixing⁵⁴ and the heat capacity of the mixtures⁵⁵ and is up to 8 K. This occurs in the region of the peak in saturation (ethanol mole fraction of ~0.16). For water, the solubility of nitrogen decreases upon increasing the temperature from 298 to 308 K,⁵⁶ and this will increase the calculated saturation accordingly showing that saturations of up to 311% are obtainable during solvent exchange of ethanol for water.

Clearly, the relative solubility of gas in the two solvents involved in solvent exchange is important for producing surface nanobubbles, as this determines the supersaturation that can be achieved. Unfortunately, as far as we can determine, the solubility of

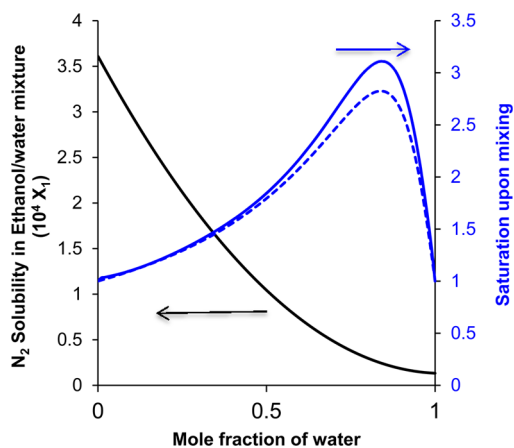


Figure 10. Calculated saturation of nitrogen produced during ethanol/water exchange for solutions initially equilibrated at 293.15 K. The nitrogen solubility as a function of mole fraction (black solid line, left-hand ordinate axis) shows a monotonic drop in solubility with increasing water content. A polynomial fit to the experimental data⁵⁶ was used to calculate the saturation level of nitrogen produced upon mixing, ignoring temperature changes induced by enthalpy of mixing (blue dashed line, right-hand ordinate axis). This is the nitrogen concentration realized when the saturated solvents of a given mole fraction are mixed, divided by the nitrogen solubility in that mixture. The saturation level reaches a maximum of 2.85 at a water mole fraction of 0.84. The temperature increase upon mixing has been calculated using the enthalpy of mixing and the heat capacity at constant pressure for the mixtures. Over the relevant temperature range, the concentration of dissolved gas in water decreases, whereas it is almost constant in ethanol, allowing the change in saturation due to temperature changes to be calculated from the change of concentration with temperature in water and the mole fraction of water. The solid blue line (right-hand ordinate axis) is the calculated saturation due to mixing of water and ethanol including the temperature changes induced by enthalpy of mixing. The saturation level reaches a maximum of 3.11 (311%) at a water mole fraction of 0.84.

gases have not been determined in mixtures of ethanol and the solvents employed in this study. Regardless, low gas solubility in the exchange solvent will favor nanobubble formation. The solubility of nitrogen has been undetectably low in some ionic solvents, whereas the solubility of oxygen is similar to that of ethanol.⁵⁷ This indicates that solvent exchange will lead to supersaturations favoring the formation of nanobubbles in EAN and PAN, and these bubbles are likely to be almost exclusively formed of nitrogen. The solubility of nitrogen in DMSO at 20 °C expressed as a mole fraction is 8.33×10^{-5} ,⁵⁸ this is ~ 6.5 times the solubility of nitrogen in water (1.274×10^{-5})⁵⁶ and ~ 4.3 times less than the solubility of nitrogen in ethanol (3.61×10^{-4}).⁵⁶ Therefore, the solvent exchange process with ethanol is likely

to lead to less supersaturation of gas in the case of DMSO and this is possibly the reason that nanobubbles were not observed in DMSO. We are unable to find solubility data to determine if this is also the case for PC. Future efforts to observe nanobubbles in nonprotic solvents should focus on alternative methods for inducing supersaturation in the solution. Solvents with three-dimensional hydrogen-bonding networks will in general exhibit higher contact angles on HOPG and have lower levels of dissolved gas. Therefore, the formation of nanobubbles by solvent exchange is more favored in these solvents. As such, it is not possible at this stage to determine if the crucial factor in observing nanobubbles in water, formamide, EAN, and PAN is the existence of a three-dimensional hydrogen-bonding network or the fact that these solvents have properties that favor the formation of nanobubbles by solvent exchange. Hydrogen-bonding networks will strongly influence interfacial properties. This may prove important in understanding both the stability and contact angles of surface nanobubbles.

CONCLUSIONS

Surface nanobubbles were observed in three non-aqueous solvents: formamide and the ionic liquids EAN and PAN. Surface nanobubbles were not observed in this study in propylene carbonate and DMSO. The difference is attributed to the existence of a 3D hydrogen bonding network in formamide, EAN, PAN, and water. This may have a direct influence on the stability or it may favor nanobubble formation during solvent exchange indirectly, through the influence of the 3D network on the physical properties of the solvent. These solvents have higher surface tensions and poorly wet the surface. Solvents that exhibit a higher contact angle on HOPG are more likely to generate nanobubbles during solvent exchange. Nanobubbles in formamide were stable for more than 120 h. These results are significant as it demonstrates that the unexplained stability and high contact angles of surface nanobubbles are not unique to aqueous systems, but may be related to the hydrogen bonding network of the solvent. The stability of nanobubbles in formamide cannot be attributed to contact line pinning as individual nanobubbles in formamide were observed to grow and shrink over a period of days and nanobubbles in formamide on a fluorinated surface were observed to be highly mobile. Nanobubbles in nonaqueous solvents exhibited anomalously high contact angles as previously observed in aqueous systems.

MATERIALS AND METHODS

Highly Ordered Pyrolytic Graphite (HOPG) and perfluorooctyltrichlorosilane (PFOTS) modified silicon surfaces were used as substrates in this investigation. HOPG was freshly cleaved

before use. PFOTS surfaces were produced by fluorination of silicon wafers. The silicon wafers were cleaned using CO₂⁵⁹ snow to remove particles, followed by RF plasma treatment at a power level of 30 W for 60 s in the presence of water vapor. A 50 μ L aliquot of ¹H,¹H,²H,²H-perfluorooctyltrichlorosilane was

mixed with 5 mL of hexadecane and 1 mL of chloroform. The surfaces were immersed in this solution for 10 min, and then washed with ethanol, dried under a stream of highly pure N_2 , and baked at 120 °C in an oven for 30 min.⁶⁰

AR grade ethanol was redistilled and stored in glass or a stainless steel pressure vessel before use. The solvents formamide (99.8%, VWR BDH Prolabo), DMSO (99.9%, Aldrich-Sigma), and propylene carbonate (PC, 99%, Merck) were used as supplied. The ionic liquids EAN and PAN (>97%, IoliTec) were dried before use. EAN and PAN (100 mL) were dried by placing them in a 250 mL round-bottom flask, gently bubbling with N_2 , heating to 120 °C for 12 h before storage in an evacuated desiccator at room temperature. In selected experiments, ethanol and formamide were degassed. This was achieved by thrice cooling the solvents using liquid nitrogen and applying a vacuum as they slowly warmed.

A multimode Nanoscope IIIa scanning probe microscope (Bruker Corporation, Santa Barbara, CA) equipped with an E scanner and a fluid cell was used in Tapping (TM) and Force–Volume (FV) Modes to obtain images of nanobubbles. A silicone O-ring was used with the fluid cell. To minimize any chance of contamination from the O-ring, it was stored in high purity ethanol for many months before use. Oxide-sharpened silicon nitride cantilevers (OMCL-TR400PSA, Olympus) with a nominal spring constant of 0.08 N/m and resonance frequency of 34 kHz were used for imaging (at an oscillation frequency of 6–35 kHz in liquids) and for force measurement. The spring constant of the cantilevers was calibrated using an MFP-3D atomic force microscope (Asylum Research, Santa Barbara, CA) by the thermal noise method⁶¹ prior to use. The cantilevers were treated with water vapor plasma (30 W, 30 s) using a custom-built plasma reactor to give a hydrophilic surface.

Nanobubbles were produced by the solvent exchange method² whereby ethanol was displaced by a nonaqueous liquid instead of an aqueous solution. The AFM fluid cell was first filled with ethanol. TM-AFM height images of the substrate were captured in ethanol before solvent exchange to confirm that no bubbles were present. The displacement of ethanol was achieved by injection of 10 mL of nonaqueous solvent over approximately 10 min using Teflon tubing and a glass syringe. As a clean glass syringe and no needle was used, we can rule out contamination by PDMS that can result from the use of disposable plastic syringes²⁵ or needles.⁶² Particular care was taken not to entrain air during solvent exchange. Imaging of nanobubbles was commenced immediately after solvent exchange.

Collecting nanobubble images in nonaqueous solvents is challenging; however, imaging can be optimized by careful adjustment of the amplitude set point and imaging gains for feedback. In general, improved images can be obtained by increasing the drive amplitude when tuning the cantilever. The image quality is sensitive to the imaging force applied by the AFM tip, so a slight change in the amplitude set point, which is the imaging amplitude normalized by the free amplitude far away from the surface in the solvent (A/A_0), can cause considerable changes in the images. An imaging force that is too large (low value of A/A_0) excessively deforms bubbles during imaging, while an imaging force that is too small results in blurred images. Effective imaging is obtained for $A/A_0 = 0.5–0.75$, where the free amplitude very far from the surface is 30–40 nm. The value of A/A_0 is lower than that used in aqueous solutions not because the surface is being tapped very hard but because the amplitude of oscillation is strongly damped near the surface in viscous solutions. That is, the free amplitude near the surface is substantially less than the free amplitude far from the surface (A_0). Images were obtained by using the highest value of A/A_0 that allowed stable images to be obtained. This causes the least deformation of the nanobubbles. AFM imaging conditions can influence the observed dimensions of nanobubbles and have a minor effect on the determined contact angle, though these effects are insufficient to explain the anomaly between measurements of the macroscopic and nanoscopic contact angles of bubbles.^{10,63–67} In measurements tracking nanobubbles over time, care was taken to minimize changes in imaging conditions and the set-point ratio was held to within 5% of the starting value.

After confirming the presence of nanobubbles on a substrate by TM-AFM imaging, the AFM tip was withdrawn and re-engaged in contact mode. Force Volume mode was then chosen and force mapping was performed on a $3 \mu\text{m} \times 3 \mu\text{m}$ scan area employing relative trigger mode. The main parameters, such as z-scan distance and threshold deflection, were then optimized according to the force curve features. Due to the high viscosity of nonaqueous solvents, the z-scan rate was set to a low value of 100 nm/s. The deflection versus z-piezo displacement curves of interest were extracted from the force image and then converted to force–distance curves in the usual manner.⁶⁸

The macroscopic contact angles of formamide, EAN, and PAN on HOPG surface were measured by an optical contact angle goniometer with automatic dispenser (CAM 200, KSV Instruments Ltd.). Sample liquid was expelled from a clean glass syringe with a Teflon stopper onto freshly cleaved HOPG. The profile of the droplet was recorded using a video camera. The nanoscopic contact angles were calculated from the AFM images of the nanobubbles, as described previously.¹⁰

Conflict of Interest: The authors declare no competing financial interest.

Acknowledgment. V Craig gratefully acknowledges the funding support of the Australian Research Council through the Discovery program.

REFERENCES AND NOTES

- Attard, P. Nanobubbles and the Hydrophobic Attraction. *Adv. Colloid Interface Sci.* **2003**, *104*, 75–91.
- Lou, S. T.; Ouyang, Z. Q.; Zhang, Y.; Li, X. J.; Hu, J.; Li, M. Q.; Yang, F. J. Nanobubbles on Solid Surface Imaged by Atomic Force Microscopy. *J. Vac. Sci. Technol., B: Microelectron. Process. Phenom.* **2000**, *18*, 2573–2575.
- Ishida, N.; Inoue, T.; Miyahara, M.; Higashitani, K. Nanobubbles on a Hydrophobic Surface in Water Observed by Tapping-mode Atomic Force Microscopy. *Langmuir* **2000**, *16*, 6377–6380.
- Craig, V. S. J. Very Small Bubbles at Surfaces—The Nanobubble Puzzle. *Soft Matter* **2011**, *7*, 40–48.
- Seddon, J. R. T.; Lohse, D.; Ducker, W. A.; Craig, V. S. J. A Deliberation on Nanobubbles at Surfaces and in Bulk. *ChemPhysChem* **2012**, *13*, 2179–2187.
- Epstein, P. S.; Plesset, M. S. On the Stability of Gas Bubbles in Liquid-Gas Solutions. *J. Chem. Phys.* **1950**, *18*, 1505–1509.
- Eriksson, J. C.; Ljunggren, S. On the Mechanically Unstable Free Energy Minimum of a Gas Bubble which is Submerged in Water and Adheres to a Hydrophobic Wall. *Colloids Surf., A* **1999**, *159*, 159–163.
- Zhang, X. H.; Chan, D. Y. C.; Wang, D. Y.; Maeda, N. Stability of Interfacial Nanobubbles. *Langmuir* **2013**, *29*, 1017–1023.
- Ducker, W. A. Contact Angle and Stability of Interfacial Nanobubbles. *Langmuir* **2009**, *25*, 8907–8910.
- Zhang, X. H.; Maeda, N.; Craig, V. S. J. Physical properties of nanobubbles on hydrophobic surfaces in water and aqueous solutions. *Langmuir* **2006**, *22*, 5025–5035.
- Berge, L. I. Dissolution of Air Bubbles by the Resistive Pulse and the Pressure Reversal Technique. *J. Colloid Interface Sci.* **1990**, *134*, 548–562.
- Zhang, X. H.; Uddin, M. H.; Yang, H. J.; Toikka, G.; Ducker, W.; Maeda, N. Effects of Surfactants on the Formation and the Stability of Interfacial Nanobubbles. *Langmuir* **2012**, *28*, 10471–10477.
- Liu, Y.; Wang, J.; Zhang, X.; Wang, W. Contact Line Pinning and the Relationship Between Nanobubbles and Substrates. *J. Chem. Phys.* **2014**, *140*, 054705.
- Liu, Y. W.; Zhang, X. R. Nanobubble Stability Induced by Contact Line Pinning. *J. Chem. Phys.* **2013**, *138*, 014706.
- Weijjs, J. H.; Lohse, D. Why Surface Nanobubbles Live for Hours. *Phys. Rev. Lett.* **2013**, *110*, 054501.
- German, S. R.; Wu, X.; An, H.; Craig, V. S. J.; Mega, T. L.; Zhang, X. Interfacial Nanobubbles Are Leaky: Permeability of the Gas/Water Interface. *ACS Nano* **2014**, *8*, 6193–6201.

17. Kikuchi, K.; Ioka, A.; Oku, T.; Tanaka, Y.; Saihara, Y.; Ogumi, Z. Concentration Determination of Oxygen Nanobubbles in Electrolyzed Water. *J. Colloid Interface Sci.* **2009**, *329*, 306–309.
18. Kikuchi, K.; Takeda, H.; Rabolt, B.; Okaya, T.; Ogumi, Z.; Saihara, Y.; Noguchi, H. Hydrogen Particles and Supersaturation in Alkaline Water From an Alkali-Ion-Water Electrolyzer. *J. Electroanal. Chem.* **2001**, *506*, 22–27.
19. Uchida, T.; Oshita, S.; Ohmori, M.; Tsuno, T.; Soejima, K.; Shinozaki, S.; Take, Y.; Mitsuda, K. Transmission Electron Microscopic Observations of Nanobubbles and their Capture of Impurities in Wastewater. *Nanoscale Res. Lett.* **2011**, *6*, 295.
20. Ebina, K.; Shi, K.; Hirao, M.; Hashimoto, J.; Kawato, Y.; Kaneshiro, S.; Morimoto, T.; Koizumi, K.; Yoshikawa, H. Oxygen and Air Nanobubble Water Solution Promote the Growth of Plants, Fishes, and Mice. *PLoS One* **2013**, *8*, e65339.
21. Wu, C. D.; Nasset, K.; Masliyah, J.; Xu, Z. H. Generation and Characterization of Submicron Size Bubbles. *Adv. Colloid Interface Sci.* **2012**, *179–182*, 123–132.
22. Safonov, V. L.; Khitrin, A. K. Hydrogen Nanobubbles in a Water Solution of Dietary Supplement. *Colloids Surf., A* **2013**, *436*, 333–336.
23. Ushikubo, F. Y.; Furukawa, T.; Nakagawa, R.; Enari, M.; Makino, Y.; Kawagoe, Y.; Shiina, T.; Oshita, S. Evidence of the Existence and the Stability of Nano-bubbles in Water. *Colloids Surf., A* **2010**, *361*, 31–37.
24. Yang, J. W.; Duan, J. M.; Fornasiero, D.; Ralston, J. Very small bubble formation at the solid-water interface. *J. Phys. Chem. B* **2003**, *107*, 6139–6147.
25. An, H.; Liu, G.; Craig, V. S. J. Wetting of Nanophases: Nanobubbles, Nanodroplets and Micropancakes on Hydrophobic Surfaces. *Adv. Colloid Interface Sci.* **2014**. DOI: 10.1016/j.cis.2014.07.008
26. Peng, H.; Hampton, M. A.; Nguyen, A. V. Nanobubbles Do Not Sit Alone at the Solid-liquid Interface. *Langmuir* **2013**, *29*, 6123–6130.
27. Liu, G. M.; Craig, V. S. J. Improved Cleaning of Hydrophilic Protein-Coated Surfaces using the Combination of Nanobubbles and SDS. *ACS Appl. Mater. Interfaces* **2009**, *1*, 481–487.
28. Chen, H. B.; Mao, H. L.; Wu, L. P.; Zhang, J.; Dong, Y. M.; Wu, Z. H.; Hu, J. Defouling and Cleaning Using Nanobubbles on Stainless Steel. *Biofouling* **2009**, *25*, 353–357.
29. Wu, Z. H.; Chen, H. B.; Dong, Y. M.; Mao, H. L.; Sun, J. L.; Chen, S. F.; Craig, V. S. J.; Hu, J. Cleaning Using Nanobubbles: Defouling by Electrochemical Generation of Bubbles. *J. Colloid Interface Sci.* **2008**, *328*, 10–14.
30. Liu, G. M.; Wu, Z. H.; Craig, V. S. J. Cleaning of Protein-Coated Surfaces Using Nanobubbles: An Investigation Using a Quartz Crystal Microbalance. *J. Phys. Chem. C* **2008**, *112*, 16748–16753.
31. Pan, G.; Yang, B. Effect of Surface Hydrophobicity on the Formation and Stability of Oxygen Nanobubbles. *ChemPhysChem* **2012**, *13*, 2205–2212.
32. Agarwal, A.; Ng, W. J.; Liu, Y. Principle and Applications of Microbubble and Nanobubble Technology for Water Treatment. *Chemosphere* **2011**, *84*, 1175–1180.
33. Kalmes, A.; Ghosh, S.; Watson, R. Charge-Stabilized Nanostructures Reduce Ischemia-Reperfusion Injury in A Pig Model *in vivo*. *Circulation* **2011**, *124*, A17400.
34. Kalmes, A. A.; Ghosh, S.; Watson, R. L. A saline-based Therapeutic Containing Charge-Stabilized Nanostructures Protects Against Cardiac Ischemia/Reperfusion Injury. *J. Am. Coll. Cardiol.* **2013**, *61*, E106–E106.
35. Modi, K. K.; Jana, A.; Ghosh, S.; Watson, R.; Pahan, K. A Physically-Modified Saline Suppresses Neuronal Apoptosis, Attenuates Tau Phosphorylation and Protects Memory in an Animal Model of Alzheimer's Disease. *PLoS One* **2014**, *9*, e103606.
36. Mondal, S.; Ghosh, S.; Watson, R.; Pahan, K. RNS60, a Novel Therapeutic, Modifies T-Helper Cells and Inhibits Experimental Allergic Encephalomyelitis: Implications for Treating Multiple Sclerosis. *Neurology* **2012**, *78*, P05.116.
37. Neto, C.; Evans, D. R.; Bonaccorso, E.; Butt, H. J.; Craig, V. S. J. Boundary Slip in Newtonian Liquids: A Review of Experimental Studies. *Rep. Prog. Phys.* **2005**, *68*, 2859–2897.
38. Karatay, E.; Haase, A. S.; Visser, C. W.; Sun, C.; Lohse, D.; Tsai, P. A.; Lammertink, R. G. H. Control of Slippage with Tunable Bubble Mattresses. *Proc. Natl. Acad. Sci. U. S. A.* **2013**, *110*, 8422–8426.
39. Seddon, J. R.; Lohse, D. Nanobubbles and Micropancakes: Gaseous Domains on Immersed Substrates. *J. Phys.: Condens. Matter* **2011**, *23*, 133001.
40. Simonsen, A. C.; Hansen, P. L.; Klosgen, B. Nanobubbles Give Evidence of Incomplete Wetting at a Hydrophobic Interface. *J. Colloid Interface Sci.* **2004**, *273*, 291–299.
41. Hayes, R.; Imberti, S.; Warr, G. G.; Atkin, R. Amphiphilicity Determines Nanostructure in Protic Ionic Liquids. *Phys. Chem. Chem. Phys.* **2011**, *13*, 3237–3247.
42. Hayes, R.; Imberti, S.; Warr, G. G.; Atkin, R. Pronounced Sponge-like Nanostructure in Propylammonium Nitrate. *Phys. Chem. Chem. Phys.* **2011**, *13*, 13544–13551.
43. Hayes, R.; Imberti, S.; Warr, G. G.; Atkin, R. The Nature of Hydrogen Bonding in Protic Ionic Liquids. *Angew. Chem., Int. Ed.* **2013**, *52*, 4623–4627.
44. Evans, D. F.; Chen, S. H.; Schriver, G. W.; Arnett, E. M. Thermodynamics of Solution of Non-Polar Gases in a Fused Salt - Hydrophobic Bonding Behavior in a Non-Aqueous System. *J. Am. Chem. Soc.* **1981**, *103*, 481–482.
45. Bako, I.; Megyes, T.; Balint, S.; Chihaia, V.; Bellissent-Funel, M.-C.; Krienke, H.; Kopf, A.; Suh, S.-H. Hydrogen Bonded Network Properties in Liquid Formamide. *J. Chem. Phys.* **2010**, *132*, 014506.
46. Izgorodina, E. I.; Forsyth, M.; MacFarlane, D. R. On the Components of the Dielectric Constants of Ionic Liquids: Ionic Polarization? *Phys. Chem. Chem. Phys.* **2009**, *11*, 2452–2458.
47. Barthel, J.; Neueder, R.; Roch, H. Density, Relative Permittivity, and Viscosity of Propylene Carbonate + Dimethoxyethane Mixtures from 25°C to 125°C. *J. Chem. Eng. Data* **2000**, *45*, 1007–1011.
48. Capelo, S. B.; Mendez-Morales, T.; Carrete, J.; Lago, E. L.; Vila, J.; Cabeza, O.; Rodriguez, J. R.; Turmine, M.; Varela, L. M. Effect of Temperature and Cationic Chain Length on the Physical Properties of Ammonium Nitrate-Based Protic Ionic Liquids. *J. Phys. Chem. B* **2012**, *116*, 11302–11312.
49. Henry, C. L.; Craig, V. S. J. Ion-specific Influence of Electrolytes on Bubble Coalescence in Nonaqueous Solvents. *Langmuir* **2008**, *24*, 7979–7985.
50. CRC. *Handbook of Chemistry and Physics*, 80th ed.; CRC Press: Boca Raton, FL, 1999–2000.
51. Li, D.; Neumann, A. W. Contact Angles on Hydrophobic Solid Surfaces and Their Interpretation. *J. Colloid Interface Sci.* **1992**, *148*, 190–200.
52. Seo, D.; German, S. R.; Mega, T. L.; Ducker, W. A. Phase State of Interfacial Nanobubbles. *J. Phys. Chem. C* **2015**, *119*, 14262–14266.
53. Ray, A. Solvophobic Interactions and Micelle Formation in Structure Forming Nonaqueous Solvents. *Nature* **1971**, *231*, 313–315.
54. Boyne, J. A.; Williamson, A. G. Enthalpies of Mixing of Ethanol and Water at 25 Degrees C. *J. Chem. Eng. Data* **1967**, *12*, 318.
55. Benson, G. C.; Darcy, P. J.; Kiyohara, O. Thermodynamics of Aqueous Mixtures of Non-Electrolytes. 2. Isobaric Heat-Capacities of Water-n-Alcohol Mixtures at 25-Degrees-C. *J. Solution Chem.* **1980**, *9*, 931–938.
56. Battino, R.; Rettich, T. R.; Tominaga, T. The Solubility of Nitrogen and Air in Liquids. *J. Phys. Chem. Ref. Data* **1984**, *13*, 563–600.
57. Anthony, J. L.; Anderson, J. L.; Maginn, E. J.; Brennecke, J. F. Anion Effects on Gas Solubility in Ionic Liquids. *J. Phys. Chem. B* **2005**, *109*, 6366–6374.
58. Dymond, J. H. Solubility of a Series of Gases in Cyclohexane and Dimethylsulfoxide. *J. Phys. Chem.* **1967**, *71*, 1829.
59. Sherman, R.; Grob, J.; Whitlock, W. Dry Surface Cleaning Using CO₂ Snow. *J. Vac. Sci. Technol., B: Microelectron. Process. Phenom.* **1991**, *9*, 1970–1977.

60. Liu, G.; Craig, V. S. J. Macroscopically Flat and Smooth Superhydrophobic Surfaces: Heating Induced Wetting Transitions up to the Leidenfrost Temperature. *Faraday Discuss.* **2010**, *146*, 141–151.
61. Hutter, J. L.; Bechhoefer, J. Calibration of Atomic-Force Microscope Tips. *Rev. Sci. Instrum.* **1993**, *64*, 1868–1873.
62. Berkelaar, R. P.; Dietrich, E.; Kip, G. A. M.; Kooij, E. S.; Zandvliet, H. J. W.; Lohse, D. Exposing Nanobubble-Like Objects to a Degassed Environment. *Soft Matter* **2014**, *10*, 4947–4955.
63. Borkent, B. M.; de Beer, S.; Mugele, F.; Lohse, D. On the Shape of Surface Nanobubbles. *Langmuir* **2010**, *26*, 260–268.
64. Walczyk, W.; Schoenherr, H. Characterization of the Interaction between AFM Tips and Surface Nanobubbles. *Langmuir* **2014**, *30*, 7112–7126.
65. Walczyk, W.; Schoenherr, H. Closer Look at the Effect of AFM Imaging Conditions on the Apparent Dimensions of Surface Nanobubbles. *Langmuir* **2013**, *29*, 620–632.
66. Song, B.; Walczyk, W.; Schoenherr, H. Contact Angles of Surface Nanobubbles on Mixed Self-Assembled Monolayers with Systematically Varied Macroscopic Wettability by Atomic Force Microscopy. *Langmuir* **2011**, *27*, 8223–8232.
67. Walczyk, W.; Schoen, P. M.; Schoenherr, H. The effect of PeakForce tapping mode AFM imaging on the apparent shape of surface nanobubbles. *J. Phys.: Condens. Matter* **2013**, *25*, 184005.
68. Ducker, W. A.; Senden, T. J.; Pashley, R. M. Direct Measurement of Colloidal Forces Using an Atomic Force Microscope. *Nature* **1991**, *353*, 239–241.